Deep Learning for 2D grapevine bud detection

Wenceslao Villegas Marset[a,*], Diego Sebastián Pérez[a,b], Carlos Ariel Diaz[a], Facundo Bromberg[a,b]

[a] *Universidad Tecnológica Nacional. Dpto. de Sistemas de la Información. Grupo de Inteligencia Artificial DHARMa, Mendoza, Argentina.*
[b] *Consejo Nacional de Investigaciones Científicas y Técnicas (CONICET), Argentina.*

Abstract

Visual inspection is a necessary task to measure relevant variables in viticulture susceptible to automation with computer vision methods. Bud detection is central for various of these tasks such as: measurement of bud sunlight exposure, autonomous pruning, bud counting, type-of-bud classification, bud geometric characterization, internode length, and bud development stage, among others. This paper presents a method for grapevine bud detection based on a *Fully Convolutional Networks Mobile-Net* architecture (**FCN-MN**). To validate its performance, this architecture was compared in the detection task with a strong method for bud detection, the scanning windows with patch classifier method, showing improvements over three aspects of detection: *segmentation, correspondence identification* and *localization*. In its best version of configuration parameters, the present approach showed a detection precision of 95.6%, a detection recall of 93.6%, a mean Dice coefficient of 89.1% for correct detection (i.e., detections whose mask overlaps the true bud), with small and nearby false alarms (i.e., detections not overlapping the true bud) as shown by a mean pixel area of only 8% the area of a true bud, and a distance (between mass centers) of 1.1 true bud diameters. These results demonstrate the advantages and limitations of our approach for real-world applications, such as *bud number*, *bud area*, and *internode length*.

Keywords: Computer vision, Fully Convolutional Network, Grapevine bud

*Corresponding author

Email addresses: `diego.villegas@alumnos.frm.utn.edu.ar` (Wenceslao Villegas Marset), `sebastian.perez@frm.utn.edu.ar` (Diego Sebastián Pérez), `carlos.diaz@frm.utn.edu.ar` (Carlos Ariel Diaz), `fbromberg@frm.utn.edu.ar` (Facundo Bromberg)

detection, Precision viticulture

1. Introduction

The present work proposes a solution for the autonomous detection of grapevine buds within 2D vineyard images captured in natural field conditions. The proposed approach is based on *Fully Convolutional Networks* (Long et al., 2015; Shelhamer et al., 2017), a deep learning model specific for computer vision applications. The present solution contributes to the historical quest for more and better quality information of different vineyard processes that affect both the grapevine productivity and grape quality.

For years, viticulturists have been producing models of the most relevant plant processes, for determining fruit quality and yield, soil profiling, or vine health, and have been gathering a wealth of information to feed into these models. Better and more efficient measuring procedures have resulted in more information, with its corresponding impact on the quality of model outcomes, while inspiring researchers to push the boundaries for producing more sophisticated models. Such information consists of a long list of variables for assessing different aspects of the plant parts involved in these processes. Examples of variables about trunks, leaves, berries, buds, shoots, flowers, bunches, and canes includes: *berry* maturity, number, weight, size and volume; *bunch* compactness, number, weight, and morphology, such as length, width, size, elongation, and volume; *bud* burst, number and size; *flower* number, *leaf* area and canopy density, *shoot* length, *trunk*'s pruning weight, among others (The Australian Wine Research Institute, a,b).

Nowadays, technology is pushing once again the possibilities regarding the quality and throughput of these measurements with improved digital and autonomous measurement procedures over manual ones. The discipline is experiencing a transition with many of its variables still being measured manually through visual inspection. This results in high labor costs that limit measurement campaigns to only small data samples which, even with the use of statistical inference or spatial interpolation techniques, limit outcome quality (Whelan et al., 1996).

In some cases, this scenario is exacerbated by the need of experts for proper measurement, such as the case of variables associated with the plant phenological stages, i.e., bud swelling, bud burst, inflorescence, flowering, veraison, and berry ripening, among others (Lorenz et al., 1995); or by a measurement procedure that requires the destruction of the plant part being measured, which prevents tracking a certain variable over time. Such is the case of the measurement of leaf area, bunch weight, berry weight and pruning weight (Kliewer and Dokoozlian, 2005).

Precision viticulture in general (Bramley, 2009), and computer vision algorithms in particular, have been growing in the last couple of decades, mainly due to their potential for mitigating these limitations (Seng et al., 2018; Matese and Di Gennaro, 2015). These algorithms come along with the promise of an unprecedented boost in the production of vineyard information as well as many expectations not only about possible improvements in the quality of the model's outcomes, but in its potential to produce better models by feeding all this information to big data algorithms.

The present work contributes to this general endeavor with an algorithm for measuring variables related to one specific plant part: the bud, an organ of major importance as it is the growing point of the fruits, containing all the plant's productive potential (May, 2000). Our contribution of autonomous bud detection not only enables the autonomous measurement of all bud-related variables currently measured by agronomists (see Table 1 for a non-exhaustive list of bud-related variables), but it also has the potential to enable the measurement of novel, yet important, variables that at present cannot be measured manually. One example is the total sunlight captured by buds, which depends on the unfeasible manual task of determining the exact location of buds in 3D space. Although the present work focuses on 2D detection, it could be easily upgraded to 3D by, for instance, integrating 2D detection into the workflow proposed by Díaz et al. (2018) .

Table 1 shows a non-exhaustive list of the main bud-related variables currently measured by vineyard managers (Sánchez and Dokoozlian, 2005; Noyce et al., 2016; Collins et al., 2020), together with an assessment of the extent to which detection contributes to their measurement. The right-most column indicates the information beyond detection, necessary to complete the measure-

Variable	(i)	(ii)	(iii)	
Bud number		x		none
Bud area	x	x		none
Type-of-bud classification	x	x		plant structure (trunk and canes)
Bud development stage	x	x		classifier over bud mask
Internode length (by bud detection)		x	x	plant structure (trunk and canes)
Bud volume				3D reconstruction
Bud development monitoring	x	x	x	
Incidence of sunlight on the bud		x	x	3D reconstruction, leaves 3D surface geometry

Table 1: A non-exhaustive list of important bud-related variables accompanied by an assessment of the extent to which detection contributes to their measurement. The right-most column indicates the information beyond detection necessary to complete the measurement, while the middle columns labeled (i), (ii), and (iii) indicate the three aspects of detection required: segmentation, correspondence identification, or localization, respectively.

ment, while the middle columns labeled (i), (ii), and (iii) indicate the specific aspects of detection required for that variable: (i) whether it requires a good *segmentation*, i.e., the discrimination of which pixels in the scene correspond to buds and which correspond to the background (non-bud); ii) a good *correspondence identification*, i.e., discrimination of bud pixels as belonging to different buds; or (iii) a good *localization*, i.e., the localization of the bud within the scene. For instance, let us take the *bud number* variable. For the bud number to coincide with the detection count. different components detected for the same bud must be bundled together as a single detection, For the *type-of-bud classification*, in addition to correctly identifying components with buds, the segmentation of the part of the image corresponding to the bud must minimize the noise produced by background pixels. Lastly, to measure the *incidence of sunlight on the bud*, localization rather than segmentation is necessary, plus the leaf 3D surface geometry.

A good detector, therefore, should be evaluated on all three aspects of segmentation, correspondence identification and localization. This is easy for our detector as its implementation first produces a segmentation mask, which is then post-processed to produce correspondence identification and localization. The specific aspects of this approach are detailed in Section 2. The analysis of detection results presented in Section 3 shows that this approach is superior to state-of-the-art algorithms for grapevine bud detection. Finally, Section 4 discusses the scope, limitations of the results obtained for bud detection, sufficiency of the performance achieved for the measurement of a selection of variables in Table 3, as well as the most important conclusions, future work and potential improvements.

1.1. Related work

A wide variety of research using computer vision and machine learning algorithms to acquire information about vineyards (Seng et al., 2018) can be found in the literature, such as berry and bunch detection (Nuske et al., 2011), fruit size and weight estimation (Tardaguila et al., 2012), leaf area indices and yield estimation (Diago et al., 2012), plant phenotyping (Herzog et al., 2014a,b), autonomous selective spraying (Berenstein et al., 2010), and more (Tardáguila et al., 2012; Whalley and Shanmuganathan, 2013). Among the outstanding computer algorithms in recent years, *artificial neural networks* have aroused great interest in the industry as a means to carry out various visual recognition tasks (Hirano et al., 2006; Kahng et al., 2017; Tilgner et al., 2019). In particular, *Convolutional Neural Networks* (**CNN**) have become the dominant machine learning approach to visual object recognition (Ning et al., 2017). Two recent studies have successfully applied visual recognition techniques based on *deep learning networks* to identify viticultural variables to estimate production in vineyards. One of them, Grimm et al. (2019), uses an FCN to carry out segmentation of grapevine plant organs such as young shoots, pedicels, flowers or grapes. The other, Rudolph et al. (2018), uses images of grapevines under field conditions that are segmented using a CNN to detect inflorescences as regions of interest, and over these regions, the *circle hough transform* algorithm is applied to detect flowers.

Several works aim at detecting and locating buds in different types of crops by means of autonomous visual recognition systems. For instance, Tarry et al. (2014) presents an integrated system for chrysanthemum bud detection that can be used to automate labour intensive tasks in floriculture greenhouses. More recently, Zhao et al. (2018) presented a computer vision system used to identify the internodes and buds of stalk crops. To the best of our knowledge and research efforts, there are at least four works that specifically address the problem of bud detection in the grapevine by using autonomous visual recognition systems. The research work by Xu et al. (2014), Herzog et al. (2014b) and Pérez et al. (2017) apply different techniques to perform 2D image detection involving different computer and machine learning algorithms. In addition, Díaz et al. (2018) introduces a workflow to localize buds in 3D space. The most relevant details of each are presented below.

Xu et al. (2014)'s study presents a bud detection algorithm using indoor captured RGB images and controlled lighting and background conditions specifically to establish a groundwork for an autonomous pruning system in winter. The authors apply a threshold filter to discriminate the background of the plant skeleton, resulting in a binary image. They assume that the shape of buds resembles corners and apply the *Harris corner detector* algorithm over the binary image to detect them. This process obtains a recall of 0.702, i.e., 70.2% of the buds were detected.

Herzog et al. (2014b)'s work presents three methods for bud detection in very advanced stages of development, i.e. when the buds burst and the first leaves emerging. All methods are semi-automatic and require human intervention to validate the quality of the results. The best result is obtained using an RGB image with an artificial black background and corresponds to a recall of 94%. The authors argue that this recall is enough to solve the problem of phenotyping vines. They also argue that these good results can be explained by the particular green color and the morphology of the already sprouting buds of approximately $2cm$.

Pérez et al. (2017) outlines an approach for the classification of bud images in winter, using *SVM* as a classifier and *Bag of Features* to compute visual descriptors. They report a recall of over 90% and an accuracy of 86% when sorting images containing at least 60% of a bud and a ratio of 20-80% of bud vs. non-bud pixels. They argue that this classifier can be used in algorithms for 2D localization of the *sliding windows* type due to its robustness to variation in window size and position. It is precisely this idea that has been reproduced in the present work to implement the baseline competitor to our approach.

Finally, Díaz et al. (2018) introduces a workflow for the localization of buds in 3D space. The workflow consists of five steps. The first one reconstructs a 3D point cloud corresponding to the grapevine structure from several RGB images. The second step applies a 2D detection method using the sliding window and patch classification technique of Pérez et al. (2017). The next step uses a voting scheme to classify each point in the cloud as a bud or non-bud. The fourth step applies the *DBSCAN* clustering algorithm to group points in the cloud that correspond to a bud. Finally, in the fifth step, the localization is performed, obtaining the center of mass coordinates of each 3D point cluster. They report a recall of 45% and a precison of 100% and a localization error of approximately $1.5cm$, or 3 bud diameters.

Although these research studies represent a great advance in relation to the problem of detecting and localizing buds, they still show at least one of the following limitations: (i) use of artificial background outdoors; (ii) controlled lighting indoors; (iii) need for user interaction; (iv) bud detection in very advanced stages of development; (v) low bud detection/classification recall, and (vi) although some of these works perform some kind of segmentation process as part of the approach, none of them aim to segment the bud or report metrics of the quality of the segmentation performed. These limitations represent a major barrier to the effective development of tools for measuring bud-related variables.

2. Materials and Methods

This section describes the main contribution of the present work, the deep learning setup FCN-MN for 2D image detection of grapevine buds captured in natural conditions. including in Subsection 2.1 details on the *encoder-decoder* transfer learning architecture. Also, in Subsection 2.2 we explain the specifics of our implementation of SW, the scanning windows and patch classification approach selected as the strongest competitor for FCN-MN, not only regarding the original workflow of Pérez et al. (2017) for the classification of the patches, but our specific proposal for bud detection based on the scanning windows technique. The section concludes with Subsection 2.3 that provides details on the training configuration of both methods, and the image collection used for both of these trainings.

2.1. Fully Convolutional Network with MobileNet (FCN-MN)

As outlined in the introduction, the approach proposes the use of computer vision algorithms to: (i) *segment* buds by *classifying* which pixels in the scene correspond to buds and which correspond to background (non-buds), (ii) *identify* bud *correspondences* by discriminating those pixels that belong to different buds in the observed scene, and (iii) *localize* each bud in the scene.

For the segmentation operation, i.e., pixel classification, the fully convolutional network introduced in (Long et al., 2015) is taken as a basis and trained for the specific problem of grapevine bud segmentation. The following section 2.1.1 describes in detail the architecture considered for these networks. The resulting fully convolutional network returns a probability map on the same scale as the original image, where the value of one pixel represents the probability that the corresponding pixel in the input image belongs to a bud. To obtain a binary mask, a classification threshold τ is applied to each pixel, classifying the pixel as bud (non-bud) if its probability is higher (lower) than τ. To identify bud correspondences, post-processing of this binary mask is performed to determine that two bud pixels correspond to the same bud, as long as they belong to the same connected component, i.e., joined by some sequence of contiguous bud pixels. Finally, there are several alternatives for the localization of objects among which are *bounding box*, *pixel-wise segmentation*, *contour* and *center of mass* of the *object* (Lampert et al., 2008). In this work the last one was considered, choosing to localize buds by the center of mass of the connected component.

2.1.1. Encoder-decoder architecture

For the pixel classifier, the three versions –32s, 16s and 8s– of the *fully convolutional networks* originally introduced by Long et al. (2015) were considered for their excellent results in many image segmentation applications (Litjens et al., 2017; Garcia-Garcia et al., 2018; Kaymak and Uçar, 2019). These networks have characteristic architectures with two distinct parts: *encoder* and *decoder* (see Figure 1).

The encoder consists of a convolutional neural network that performs a *downsampling* of an input image into a feature set, by means of convolution operations to produce a set of *feature maps*, i.e., an abstract representation of the image that captures semantic and contextual information, but discards fine-grained

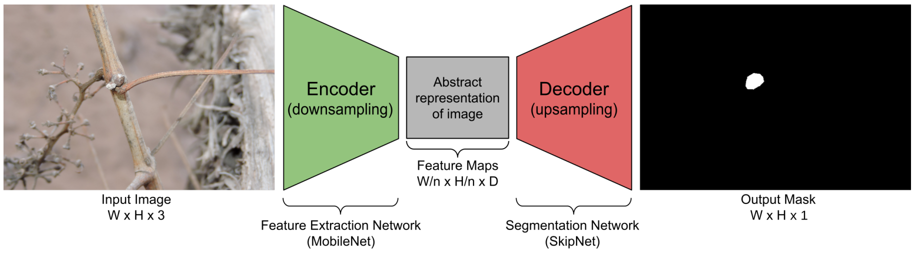

Figure 1: Diagram of the FCN-MN network architecture proposed in this work, based on the fully convolutional network proposed by Shelhamer et al. (2017), replacing its feature extraction encoder with the MobileNet network Howard et al. (2017), which produces feature maps with a downsampling factor of n. As a decoder for the production of the segmentation map, the SkipNet network Siam et al. (2018) is used, implementing variants 32s, 16s and 8s.

spatial information. These operations reduce the spatial dimensions of the image as one goes deeper into the network, resulting in feature maps 1/n the size of the input image, where n is the downsampling factor. The decoder is an *upsampling* subnet, which takes the low-resolution feature map and projects it back into pixel space, increasing the resolution to produce a segmentation mask (or dense pixel classification) with the same dimensions as the input image. This operation is implemented as a network of transposed convolutions with trainable parameters, also known as upsampling convolutions (Shelhamer et al., 2017).

To refine the segmentation quality, connections that go beyond at least one layer of the network, called *skip connections*, are often used to transfer local spatial information from the internal encoder layers directly to the decoder. In general, these connections improve segmentation results, since they mitigate the loss of spatial information by allowing the decoder to incorporate information from internal feature maps. Their impact may vary depending on the proposed skip architecture. In Long et al. (2015), three skip architectures are proposed: 32s without information from internal encoder layers; 16s that adds spatial information from deep encoder layers; and 8s that adds spatial information from deep and less deep encoder layers. The details of these architectures are beyond the scope of this paper, but can be found in Long et al. (2015) and Shelhamer et al. (2017). Since the results reported in the literature are not conclusive regarding which architecture is better, in this work all three alternatives are considered.

In spite of having achieved excellent results in practice, these architectures carry a significant load of computational resources. With this in mind, in this work the VGG encoder of Simonyan and Zisserman (2015), originally proposed by Long for fully convolutional networks, was replaced by the MobileNet network of Howard et al. (2017). This network stands out for having only 4.2 million parameters against the 138 million parameters of VGG, allowing the training and testing process to be considerably faster, with a much lower memory requirement, while maintaining performance. It is due to these changes that for the rest of the paper these networks are referred to as **FCN-MN**. The use of MobileNet as an encoder in the fully convolutional networks of Long et al. (2015) is not new, but had already been proposed for the 8s architecture by Siam et al. (2018) in his SkipNet architecture. Technically, Siam et al. (2018)'s proposal is extremely simple; motivating us to extend it to the 16s and 32s architectures originally proposed by (Long et al., 2015).

2.2. Sliding Windows detector

This section describes the approach proposed by Pérez et al. (2017) for the classification of bud images and our implementation for detection based on the sliding windows described in the original paper, denoted hereon by **SW**. The approach follows three steps: (i) it applies the sliding windows algorithm to an image to extract patches (sub-images or rectangular regions); (ii) it classifies (all pixels of) each patch into either bud or non-bud, using the algorithm presented in Pérez et al. (2017); and (iii) it produces the final segmentation mask using a voting scheme. Details of each step are provided below.

Sliding windows techniques comprise a family of algorithms widely used in the past as part of various approaches to object localization with bounding boxes (Divvala et al., 2009; Wang et al., 2009; Chum and Zisserman, 2007; Ferrari et al., 2007; Dalal and Triggs, 2005; Rowley et al., 1996). In these algorithms, each image is scanned densely from one end of the image (e.g. upper left corner) to the other end (e.g. lower right corner) by a rectangular sliding window in different scales and different displacements, extracting sub-images or patches from the original image. In this work, 10 window sizes of equal height and width are defined, namely 100, 200, 300, 400, 500, 600, 700, 800, 900 and

1000 pixels, with a horizontal displacement of 50% the width of the window and a vertical displacement of 50% the height of the window, resulting in a 50% overlap between both horizontally and vertically contiguous patches. As a result, each pixel of the image simultaneously belongs to 4 patches. These values were chosen on the basis of the robustness analysis of the classifier presented by Pérez et al. (2017) for the window geometry. This analysis shows that the classifier is robust for patches that contain at least 60% of the pixels of a bud, and whose area is composed of at least 20% bud pixels. If we consider extreme cases, i.e., the smallest bud diameter of 100px and the largest of 1600px, window sizes of 100px and 1000px could contain at least 60% of the pixels of a bud. In addition, using a 50% displacement, it is guaranteed that at least one patch will contain more than 20% bud pixels, 50px and 500px, respectively. The authors argue that a sliding window detection algorithm could easily propose a scheme for choosing window size and displacement to ensure that at some point in the scan the window meets the robustness requirements. However, no details are given on how to implement it, so in this paper we only report results for fixed window sizes and 50% displacement. Since the collection of buds have a variable diameter, not all window sizes will be able to satisfy the robustness requirements for all patches, but the results can still be useful to make a comparison with the FCN-MN approach.

The second step in this approach is to determine whether a patch is a bud or non-bud type. The classifier in Pérez et al. (2017) takes the patches produced by the sliding windows and, for each patch, it performs the following operations: (i) it computes low-level visual features using the *Scale Invariant Feature Transform* or SIFT algorithm (Lowe, 2004); (ii) it builds a high-level descriptor for each patch using the *Bag of Features* or BoF algorithm of Csurka et al. (2004) over the SIFT features from the previous step; and (iii) it determines the class of each patch using the BoF descriptor as input to a classifier built using the *Support Vectors Machine* algorithm (Vapnik, 2013). Details of the training of this classifier are in Section 2.3.3.

Finally, the third step of the approach builds the binary mask of bud pixels. The mask is constructed through a voting scheme where each pixel gets one vote for each patch classified as a bud that contains it, where the maximum of votes is 4 given that 4 is the number of patches a pixel belongs to. A pixel is then added to the positive (bud) mask if it gets more than ν votes, where ν is a user given configuration parameter.

2.3. Model training

This section provides details of the training process for each approach. In order to contrast both approaches they have been designed to receive the same type of input, i.e., an image of a viticultural scene, and to produce the same outputs, i.e., a binary mask of the same size as the original image whose positive pixels represent bud-type pixels. This allows both to be trained with the same image collection, which is described in the following section, followed by model-specific training details.

2.3.1. Image collection

The image collection used in this study is the same collection originally used in Pérez et al. (2017), which has been downloaded from `http://dharma.frm.utn.edu.ar/vise/bc` as indicated by the authors. The complete collection consists of 760 images captured in winter in natural field conditions. However, in this work, only the 698 images containing exactly one bud were taken. Each image is accompanied by the ground truth, that is, a mask of the manual segmentation of the bud. These images and their masks were used during the training and evaluation of the detection models. For this purpose, the image collection was separated into two disjoint subsets: the *train set* with 80% of the images and the *test set* with the remaining 20%. This resulted in a train set of 558 images and a test set of 140 images, both with their respective ground truth masks.

2.3.2. FCN-MN training

The 558 images reserved for this purpose were used to train this approach. These images have different resolutions; however, the three proposed FCN-MNs require a fixed size entry. Therefore, all images (including their masks) were scaled to a resolution of 1024×1024 pixels using a bilinear interpolation method (Han, 2013). In addition, for the train set images, the pixel RGB intensity values were scaled from [0.255] to [-1, 1].

Given the small number of images in the train set, two techniques widely used in practice were employed to achieve robust training: *transfer learning* (Pan and Yang, 2009) and *data augmentation* (Shorten and Khoshgoftaar, 2019). The transfer learning process was carried out as follows: (i) the original MobileNet network proposed by Howard et al. (2017) was implemented; (ii) the network was initialized with the parameters pre-trained on the ImageNet benchmark dataset (Kornblith et al., 2019); (iii) the MobileNet multi-class classification layer was replaced by a binary classification layer; (iv) the network was trained as a bud and non-bud patch classifier in an analogous way to SVM training using the same balanced patch train set used for training SW, after scaling all its images to 224×224 pixels; and (v) the parameters obtained in the previous step were used to initialize the encoder of our FCN-MN. The data augmentation process was applied on the fly during training. For each train set image, 200 new images (111600 in total) were generated by simultaneously applying the following seven operations, whose values were taken at random with uniform probability: *rotation* of up to 45°; *horizontal shifting* of up to 40%; *vertical shifting* of up to 40%; *shear* of up to 10%; *Zoom* of up to 30%; *horizontal flip* and *vertical flip*.

For the training of the three FCN-MN variants –8s, 16s, and 32s– it is required to specify the *optimization method* and *dropout* value, two parameters typically defined by the user. In this work, the optimization methods considered were: *Adam* with learning rate 0.001, $beta1 = 0.9$ and $beta2 = 0.999$; *RMSProp* with learning rate 0.001 and $\rho = 0.9$; and *Stochastic Gradient Descent* with learning rate 0.0001 and $momentum = 0.9$. For the dropout case, two values were considered: 0.5 and 0.001. These values were pre-selected by preliminary experiments not discussed here.

The best combination of optimization method and dropout was determined in training time over a validation set, using the *4-fold cross validation* approach by 60 epochs and batchsize equal to 4, varying over the three optimization methods and the two dropout values. The values selected were those that maximize the mean of Jaccard's *Intersection-over-Union* (IoU) (Jaccard, 1912), a typical assessment measure in segmentation problems. For each combination of optimizer and dropout values the simple mean is reported over 12 IoU corre-

	Mean IoU	
Optimizer	**Dropout = 0.001**	**Dropout = 0.5**
RMSprop	0.44253	0.3117
Adam	0.240277	0.315714
SGD	0.000886	0.00151

Table 2: For each combination of optimizer and dropout values the simple mean is reported between 12 IoU corresponding to the 3 variants considered in each of the 4 folds.

sponding to the 3 variants considered in each of the 4 folds. It can be observed in Table 2 that the combination of parameters with which the highest average IoU is reached is RMSProp with a dropout of 0.001. Using these parameters, the 8s, 16s, and 32s architectures were trained over 200 epochs and batch size of 4

2.3.3. SW approach training

The training for this approach is conducted in the same way as for the original workflow proposed in Pérez et al. (2017). This involves training a binary classifier to learn the concept of bud versus non-bud from a collection of rectangular patches that may or may not contain a bud. During the training, bud patches must be regions that perfectly circumscribe the bud while non-bud patches must be regions that contain not a single bud pixel (see Figure 2). Therefore, to build the patch collection, the 558 images and their masks were processed following the same protocol as in Pérez et al. (2017), obtaining a total of 558 patches circumscribing each bud (one per image), and more than 25000 non-bud patches (the non-bud area is much larger than the area occupied by a bud in the image). The size of these patches is variable, with resolutions between 0.1 and 2.6 megapixels for the 100×100 to 1600×1600 pixels patches.

From this collection of patches, a balanced patch train set was created, with 558 patches for each class, where non-bud patches were taken at random from the collection of 25000 background patches. The training was performed as detailed in the pipeline proposed by Pérez et al. (2017): (i) all SIFT descriptors were extracted from the train set; (ii) BoF was applied with a vocabulary size equal to 25; and (iii) the SVM classifier was trained on the BoF descriptors of

Figure 2: Collection of patches used in this work. The first and second rows correspond to bud patches and non-bud patches, respectively. Image extracted from Pérez et al. (2017).

each patch using a *Radial Basis Function* kernel, where the value of the γ and C parameters was established by means of a 5-fold cross-validation on the same value ranges: $\gamma = \{2^{-14}, 2^{-13}, \ldots, 2^{-7}\}$ and $C = \{2^5, 2^6, \ldots, 2^{14}\}$.

3. Experimental results

In this section we present a systematic evaluation of the quality of our proposed FCN-MN procedure for bud detection. According to the discussion in the introduction, detection can be decomposed into the three aspects *segmentation*, *correspondence identification*, and *localization* that affect the relevant bud-related variables listed in Table 1.

First, inthe following subsection, we present metrics that quantify the quality of these aspects, followed by subsection 3 that presents the results for the metric values obtained for different experiments over the image test set.

3.1. Performance metrics

3.1.1. Correspondence identification metrics

Detection of buds is the result of two steps: (i) thresholding of the output masks into a *binary mask*. For FCN-MN this is done by keeping all pixels of the probabilistic mask with values higher than τ, and for SW this is done keeping all pixels that belong to at least ν positive patches, and (ii) considering each *connected component* of the binary mask as exactly one detected bud.

The correspondence identification metrics measure in what amount these detections are *correct* or *incorrect*, by first corresponding detections with true buds whenever the detected and true masks overlap on at least one pixel. The best case scenario occurs when each detected bud overlaps exactly one true bud. In some cases this correct detection could be splitted with more than one detected component overlapping the same true bud. But still it is clear to which true bud these components correspond to. For images with more than one true bud, the correspondence identification may become unclear when it occurs that a single detected component overlaps more than one true bud, resulting in the large amount of possible detection metrics defined in Oguz et al. (2017). To simplify the analysis, our image collection contains a single bud per image, resulting in the following simplified list of possible metrics:

- **Correct Detection** (CD) are *true positive* cases where there is exactly one component per image overlapping the true bud. Here, CD counts all images satisfying this condition.
- **Split** (S) are *true positives* as well, but with more than one component overlapping some true buds. We report it separately to assess the problem of double counting. Here S counts the number of true buds for which this occurs, which in our case of one true bud per image, corresponds to the number of images for which this occurs.
- **False Alarm** (FA) is equivalent to a *false positive* situation and corresponds to detected connected components not overlapping the true bud. This measure counts the total number of such components over all images.
- **Detection Failure** (DF) is equivalent to a *false negative* situation when the detection mask presents no connected components. It counts one for each image that satisfies this condition.

To quantify the correspondence identification quality one could simply report these quantities counted over the test set, with the best case consisting in a CD value equal to the cardinality of this set. However, determining the overall correspondence identification quality from the analysis of four quantities can become rather complicated.

One alternative is reporting precision and recall, denoted as P_D and R_D, and referred to as *detection-precision* and *detection-recall* to distinguish them from the segmentation precision and recall defined further down. For that, the fact that there are two different true positive counts, CD and S, needs to be addressed first. This is solved by first counting as true positives not only the CD type of images, but also S, i.e., any image with either a correct detection or a split case is counted as one true positive, resulting in:

$$P_D = \frac{true\ positives}{true\ positives + false\ positives} = \frac{CD + S}{CD + S + FA},$$

$$R_D = \frac{true\ positives}{true\ positives + false\ negatives} = \frac{CD + S}{CD + S + DF}.$$

Then, the split type of errors is accounted for by explicitly reporting S.

Given these quantities, we also report the *F1-measure*, denoted $F1$, computed as their harmonic average $F1 = 2 \times \frac{P_D \times R_D}{P_D + R_D}$.

3.1.2. Segmentation metrics

Correspondence identification metrics, although informative, relies on the overlap between detected and true buds, regardless of how minimal the overlap is. This could miss several possible pixel-wise detection errors, resulting in rather coarse comparisons between competing detection algorithms. For instance, a correct detection could present a very small overlap with the true bud, with many or even a majority of the true bud pixels missing (i.e., several *false negative* pixels), or it could be erroneously reporting several pixels as bud pixels (i.e., several *false positive* pixels). Clearly, the best case scenario would be a case of correct detection with no false negative or positive pixels that would visually correspond to a perfect overlap between the detected connected component and the true bud.

A pixel-wise comparison of the masks could help to assess split quality as well. The best split, for instance, would be one completely enclosed within the true mask –i.e., with none of its connected components presenting false positive pixels–, while covering as much of the true bud mask as possible, i.e., presenting just enough false negatives to disconnect its components. Finally, a false alarm case, presenting only false positive pixels, could be further assessed by the quantity of pixels in the component.

The community has proposed several metrics to quantify segmentation errors. The most obvious ones are those that report the *fraction* of the whole image corresponding to *true positive*, *false positive*, and *false negative* pixels; denoted TPF, FPF, and FNF, respectively. Again, one can simplify the analysis by considering pixel-wise precision and recall, denoted as P_S and R_S and referred to as *segmentation precision*, *segmentation recall*, defined formally as:

$$\begin{aligned} P_S &= TPF/(TPF + FPF) \\ R_S &= TPF/(TPF + FNF), \end{aligned}$$

and their weighted harmonic mean, the well-known *F-measure*, defined formally as $2 \times P_S \times R_S/(P_S + R_S)$. The segmentation F-measure has been proposed independently by Dice (1945); thus, usually referred to as the *Dice measure*. A common alternative to the Dice measure is the Jaccard's *intersection-over-union* (Jaccard, 1912) defined by $TPF/(TPF + FPF + FNF)$. In this work we report only the Dice measure, using the IoU only for model selection as explained in Section 2.3.2.

One could refine these metrics by applying them, not to the whole mask, but to the individual correspondence identification cases; for instance, by reporting the mean Dice measured over all correctly detected components. Or else, by refining the assessment of how bad a split is, one could report the mean Dice measure to all components of some split or the mean Dice measure over all split components of all split images.

The case of false alarms is rather monotonous and not very informative with zero precision and recall for all such components. A pixel-wise assessment of the gravity of a false alarm requires a specific quantification of the number of false positive pixels. One could simply consider the FPF, the fraction of all the false positive image pixels. Instead, we considered a normalization against bud size to be more informative, resulting in the *normalized area*, denoted as NA and defined formally as *the area of the component normalized by the area of the (single) true bud in the image*, with a component's area corresponding to its total number of pixels.

3.1.3. Localization metrics

As a localization metric we propose the *normalized distance*, denoted as ND, defined formally as *the distance between the center of mass of the component and the center of mass of the true bud, divided by the diameter of the true bud.* with the bud's diameter corresponding to the maximum distance between any two border points of the true bud.

3.2. Results

We proceed now to assess the validity of our main hypothesis that FCN-MN is a better detector than its SW counterpart, over each of the metrics defined in the previous section.

For a thorough comparison, several cases for each algorithm were considered: training 27 FCN-MN detectors and 40 SW detectors over the training set of 558 images, one for each combination of their respective hyper-parameters. For FCN-MN, these hyper-parameters are the three architectures –8s, 16s, and 32s– and the 9 values $\{0.1, 0.2, \ldots, 0.9\}$ for the binarization threshold τ. For SW, in turn, these hyper-parameters are the 10 patch sizes $\{100, 200, \ldots, 1000\}$ and the 4 values $\{1, 2, 3, 4\}$ of the voting threshold ν. Then, each of these 67 models were evaluated over the 140 images reserved for testing purposes, obtaining for each image the detection components.

Table 3 shows the results for the best detectors of each algorithm, reporting all performance metrics of the three aspects of detection over all detected components over the 140 test images: correspondence identification, segmentation and localization. The first column shows the label of the selected detectors, with the subscript indicating the architecture and patch size for the case of FCN-MN and SW, respectively; and the superscript indicating the thresholds τ and ν, respectively.

The table includes all metrics defined in Section 3.1 required for a thorough comparison of FCN-MN against SW. First, four correspondence identification metrics are included: detection precision P_D, detection recall R_D, the F1-measure $F1$, and S the total count of test images with splitted detections. Followed by the seven segmentation metrics: the mean and standard deviation (in parenthesis) segmentation precision, segmentation recall, and the Dice measure over correct detections and splits, denoted in the table by P_S^{CD}, R_S^{CD} and $Dice^{CD}$ for correct detections and P_S^S, R_S^S and $Dice^S$ for splits; plus the mean and standard deviation of the normalized area for false alarms denoted NA. We remined the reader that the segmentation metrics for splits are computed over the union of all split components over each image. Finally, the table reports the normalized distance ND. We could consider here a separate report for the different correspondence identification classes. However, as they overlap the true bud, correctly detected and splitted components should be so close to the true bud that we found no need to present their values in detail, reporting only their minimum and maximum ND values instead of a whole column in the table. The table then includes the column ND, with each cell reporting the mean and standard deviation (in parenthesis) *normalized distance* ND over all false alarm components of all test images.

The table is a summary, as it includes only a subset of all 27 FCN-MN cases and a subset of all 40 SW cases. A detector was considered for inclusion in the table if, when compared to its counterparts of the same algorithm, it resulted in the highest value for at least one of the metrics. The corresponding cell was marked in bold in the table. For instance, the detector FCN-MN$_{16s}^{0.8}$ has been included because its detection precision P_D of 97.7% is the largest among the detection precision of all 27 FCN-MN detectors. Similarly, the detector SW$_{1000}^{1}$ has been included because its precision $P_D = 67.0\%$ is the largest among all 40 SW detectors.

The table shows a clear improvement of FCN-MN over SW. For all metrics, the best FCN-MN detector (bolded) improves (or ties) over the best SW detector (bolded) represented in the table by underlying the detector with the best metric. The exception is the two segmentation recalls R_S^{CD} and R_S^S for correct detections and splits, for which the SW case has a better (larger) mean, 98.8% versus 99.9% for correct detections and 74.7% versus 78.6% for the split case; and the total split count S, with the best case for FCN-MN being 1 and 0 for the best SW case. These improvements are not statistically significant, however, due to the large standard deviations of the FCN-MN cases, of 3.4 and 8.1 for correct detections and splits, respectively, resulting in (statistically) overlapping values.

In some cases, the improvements of FCN-MN over SW are overwhelming. For instance, for detection-precision P_D, correctly detected segmentation-precision P_S^{CD}, and split segmentation-precision P_S^S, the FCN-MN over SW improvements are 97.7% versus 67.0%, 98.1% versus 46.5%, and 99.9% versus 67.5%, respectively. In addition, for the NA and ND (of false alarms), where a smaller value is better, the FCN-MN versus SW improvements are 0.04 versus 0.22 and 1.1 versus 6.0, respectively.

As mentioned, we omitted in the table the mean normalized distances for correct detections and splits, but for completeness let us present their minimum and maximum values. For each FCN-MN and SW detector we computed the resulting mean normalized distance over all correctly detected components in the test set, on one hand, and over all split components in the test set on the other. Among all FCN-MN detectors, the *minimum* and *maximum* mean are 0.049(0.055) and 0.081(0.145), respectively. Similarly, the minimal and maximal pair for the splitted components is 0.261(0.179) and 0.429(0.066), respectively. As predicted, all rather small, with both the minimum and maximum mean distance falling within one diameter of a true bud, for all cases. For the SW detectors, the min/max pair of mean normalized distances for the correctly detected components is 0.383(0.2089)/1.352(1.43), and for splits components is 0.329(0.206))/1.152(0.023), respectively. As can be observed, again FCN-MN shows an improvement over SW, with no statistically significant overlap of their min/max interval for the correct detections, and a minor statistically significant overlap for the splits (where the maximum value $0.429 + 0.066$ for FCN-MN, is overlapping the minimum value $0.329 - 0.206$ of SW).

3.2.1. Detailed analysis of correspondence identification metrics

Graphically, one could expect a better combined analysis of detection-precision and detection-recall than could be obtained by comparing the F1-measure. This is shown as a scatter plot in Figure 3, a graphical representation of a non-summarized version of the second and third columns of Table 3. Each dot in the plot is located according to the detection-precision and detection-recall, and the color black or white, whether it corresponds to an FCN-MN or an SW detection model.

Detector	P_D	R_D	$F1$	S	P_S^{CD}	R_S^{CD}	$Dice^{CD}$	P_S^S	R_S^S	$Dice^S$	NA	ND
FCN-MN$^{0.5}_{8s}$	75.4	98.6	85.4	2	91.0 (11.3)	90.2 (11.7)	**89.6 (10.3)**	96.6 (2.2)	73.1 (17.6)	**82.1 (10.2)**	0.26 (0.69)	3.72 (4.64)
FCN-MN$^{0.9}_{8s}$	90.1	97.1	93.5	8	**98.1 (6.0)**	68.3 (21.1)	77.9 (19.6)	98.7 (3.0)	57.4 (18.4)	70.8 (13.6)	0.24 (0.5)	3.8 (5.66)
FCN-MN$^{0.1}_{16s}$	71.3	**100**	83.2	6	75.7 (13.1)	95.4 (14.7)	83.1 (13.5)	83.1 (8.9)	54.1 (21.9)	61.9 (17.5)	0.12 (0.44)	5.27 (6.53)
FCN-MN$^{0.4}_{16s}$	87.0	96.4	91.5	**1**	87.7 (12.1)	89.8 (18.2)	87.0 (15.6)	96.7 (0.0)	37.0 (0.0)	53.5 (0.0)	**0.04 (0.09)**	3.8 (5.08)
FCN-MN$^{0.6}_{16s}$	95.6	93.6	94.6	3	92.2 (8.7)	88.2 (13.3)	89.1 (10.7)	99.4 (0.6)	16.2 (10.6)	26.6 (16.8)	0.08 (0.11)	**1.1 (0.65)**
FCN-MN$^{0.8}_{16s}$	**97.7**	92.1	**94.9**	4	95.8 (7.0)	81.6 (14.6)	87.0 (10.7)	99.7 (0.3)	34.2 (32.6)	43.9 (33.1)	0.1 (0.12)	1.28 (0.95)
FCN-MN$^{0.9}_{16s}$	**97.7**	91.4	94.5	4	97.6 (5.6)	74.5 (16.5)	83.1 (12.8)	**99.9 (0.1)**	31.8 (27.9)	41.6 (34.0)	0.07 (0.11)	1.33 (0.9)
FCN-MN$^{0.1}_{32s}$	35.4	**100**	52.2	8	67.4 (14.0)	**98.8 (3.4)**	79.1 (11.0)	86.0 (9.4)	73.4 (19.6)	77.1 (10.4)	0.14 (0.66)	4.62 (5.59)
FCN-MN$^{0.2}_{32s}$	50.9	**100**	67.5	10	73.9 (13.6)	98.1 (3.8)	83.5 (10.1)	92.2 (5.4)	53.4 (25.8)	63.6 (19.3)	0.17 (0.55)	4.33 (6.17)
FCN-MN$^{0.3}_{32s}$	49.8	**100**	66.5	10	79.1 (13.2)	95.5 (10.5)	85.2 (11.8)	88.5 (9.7)	61.0 (35.1)	65.8 (28.2)	0.1 (0.39)	3.68 (5.62)
FCN-MN$^{0.6}_{32s}$	68.5	99.3	81.1	16	89.0 (11.5)	89.1 (11.3)	88.1 (9.6)	92.4 (7.7)	**74.7 (28.1)**	78.1 (24.0)	0.11 (0.3)	2.95 (4.36)
SW$^{1}_{100}$	9.4	**100**	**17.2**	28	24.6 (17.7)	86.7 (19.5)	33.6 (15.1)	57.9 (28.2)	24.8 (16.8)	27.9 (13.8)	1.08 (3.2)	7.68 (6.02)
SW$^{3}_{100}$	14.6	93.1	25.3	40	42.4 (26.4)	56.8 (29.9)	**39.9 (19.7)**	55.5 (32.2)	24.8 (18.1)	26.0 (15.6)	0.31 (0.96)	6.45 (6.19)
SW$^{4}_{100}$	19.5	87.4	31.9	49	**46.5 (29.3)**	39.2 (28.9)	33.9 (21.1)	49.0 (29.0)	20.1 (13.7)	24.1 (14.0)	**0.22 (0.57)**	**6.0 (6.56)**
SW$^{1}_{200}$	20.0	**100**	33.3	12	16.6 (12.5)	94.9 (13.5)	25.9 (14.2)	49.3 (26.4)	40.2 (17.4)	36.8 (11.9)	5.13 (19.3)	7.56 (5.35)
SW$^{3}_{200}$	26.0	98.6	41.1	19	29.9 (17.0)	74.7 (27.3)	38.5 (17.0)	**67.5 (32.7)**	16.5 (8.9)	24.2 (11.9)	1.69 (3.15)	8.94 (6.22)
SW$^{1}_{300}$	26.9	**100**	42.4	2	13.7 (13.6)	97.0 (9.6)	21.6 (15.5)	55.0 (11.8)	48.1 (1.1)	**50.8 (4.5)**	7.79 (20.5)	6.83 (4.44)
SW$^{1}_{400}$	32.7	**100**	49.3	2	10.5 (11.7)	98.7 (9.3)	17.2 (15.3)	42.6 (10.1)	61.9 (11.6)	50.4 (10.9)	11.59 (24.05)	7.12 (4.15)
SW$^{2}_{400}$	34.6	**100**	51.4	4	15.6 (15.1)	94.5 (13.3)	23.8 (15.6)	48.7 (27.6)	36.0 (4.6)	38.6 (13.1)	9.54 (26.13)	7.88 (4.89)
SW$^{1}_{500}$	40.2	**100**	57.3	1	8.40 (9.7)	**99.9 (4.9)**	14.2 (13.8)	17.9 (0.0)	**78.6 (0.0)**	29.2 (0.0)	17.39 (30.07)	7.22 (4.04)
SW$^{2}_{500}$	38.6	**100**	55.7	1	13.5 (14.0)	95.2 (14.5)	21.0 (16.0)	35.2 (0.0)	45.9 (0.0)	39.8 (0.0)	17.19 (39.07)	7.56 (4.42)
SW$^{1}_{600}$	43.5	**100**	60.6	**0**	6.9 (7.8)	98.5 (10.7)	12.0 (12.0)	nan (nan)	nan (nan)	nan (nan)	25.48 (48.45)	7.72 (4.3)
SW$^{2}_{600}$	41.7	**100**	58.8	1	10.4 (10.6)	93.7 (18.9)	17.2 (14.4)	19.7 (0.0)	27.2 (0.0)	22.9 (0.0)	20.41 (38.32)	7.92 (4.38)
SW$^{1}_{700}$	50.6	**100**	67.2	**0**	5.6 (6.5)	98.6 (12.0)	9.9 (10.3)	nan (nan)	nan (nan)	nan (nan)	31.95 (64.36)	7.75 (4.45)
SW$^{1}_{800}$	56.7	**100**	72.4	**0**	5.1 (6.6)	97.7 (11.0)	9.0 (10.4)	nan (nan)	nan (nan)	nan (nan)	44.53 (71.52)	7.7 (4.06)
SW$^{2}_{800}$	49.6	99.2	66.1	**0**	8.3 (9.4)	95.0 (15.9)	13.9 (13.2)	nan (nan)	nan (nan)	nan (nan)	30.52 (46.45)	7.82 (4.1)
SW$^{1}_{900}$	64.3	**100**	78.3	**0**	4.2 (5.7)	94.7 (19.0)	7.5 (9.2)	nan (nan)	nan (nan)	nan (nan)	48.16 (80.31)	7.9 (4.35)
SW$^{3}_{900}$	42.2	92.4	58.0	**0**	15.0 (14.8)	81.5 (28.9)	22.7 (16.8)	nan (nan)	nan (nan)	nan (nan)	17.97 (29.56)	7.65 (4.67)
SW$^{1}_{1000}$	**67.0**	**100**	**80.2**	**0**	3.7 (4.7)	95.3 (18.3)	6.8 (7.9)	nan (nan)	nan (nan)	nan (nan)	57.83 (84.87)	7.91 (4.3)
SW$^{2}_{1000}$	56.7	98.3	71.9	**0**	6.3 (6.9)	93.8 (19.1)	11.1 (10.9)	nan (nan)	nan (nan)	nan (nan)	47.26 (68.92)	7.98 (4.44)

Table 3: Correspondence identification, segmentation and localization metrics for the best FCN-MN and SW detection models. Each column shows two bolded cells corresponding to the cell with the best metric among all FCN-MN rows and the cell with best metric among SW rows. The larger of the two has been underlined, representing the best among all combined models, i.e., the best of the column. Columns P_D, R_D, $F1$ and S show results for the *Correspondence identification metrics* detection precision, detection recall, F1-measure and number of images with splits, respectively: Columns P_S^{CD}, R_S^{CD} and $Dice^{CD}$ (resp. P_S^S, R_S^S and $Dice^S$) correspond to the *segmentation metrics* mean segmentation precision, mean segmentation recall, and mean Dice measure over all correctly detected components (resp. split components); and Columns NA and ND show the mean NA and mean ND over all false alarm components.

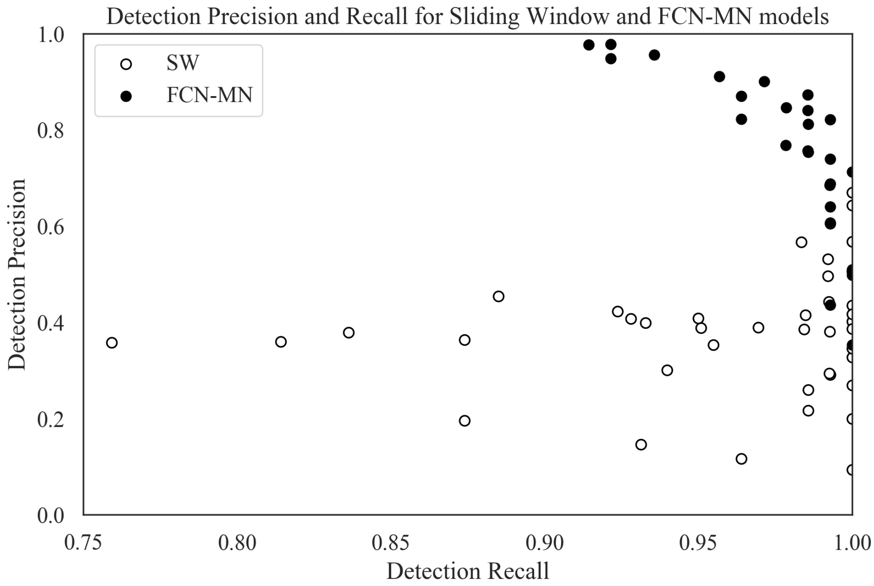

Figure 3: Precision-Recall scatterplots of the second and third columns of Table 3 discriminating the results for FCN-MN and SW with black and white dots, respectively. Each dot represents the detection-precision P_D and detection-recall R_D computed over all test images, for some particular configurations of hyper-parameters among all models (27 for FCN-MN and 40 for SW).

The graph reinforces the clear and undisputed improvements of FCN-MN over SW already shown in the table, with similar detection-recalls, but larger detection-precisions over most scenarios.

Detection-precision and detection-recall are computed over a combination of correctly detected and splitted components. To easily assess the impact of the split cases, Figure 4 shows the S values corresponding to the fifth column of a (non-summarized version of) Table 3 in the form of a histogram, with bins representing values of S and the bars for that bin representing the proportion of models that resulted in that value of S. Black and white bars discriminate the cases for FCN-MN and SW, respectively. For instance, the first bin indicates that approximately 54% of the FCN-MN models and approximately 62% of the SW models resulted in a total number splits of less than 5. Overall, the FCN-MN distribution is slightly more concentrated in the lower number of splits than the SW distribution, but in general both algorithms compare fairly, with no clear

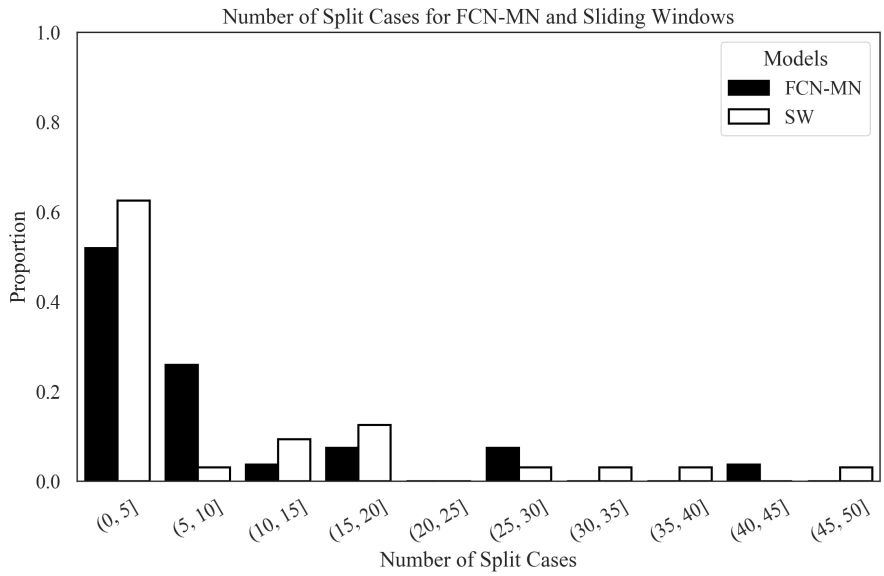

Figure 4: Histogram reporting the distribution of S for FCN-MN and SW in black and white bars, respectively. Each bar represents the proportion among all models (27 for FCN-MN and 40 for SW) that contains the number of splits indicated by the bin label. For instance, the first (from left to right) white bar indicates that almost 62% out of the 40 SW models contains between 0 and 5 splits.

contender when compared with the average number of splits they produce.

3.2.2. Detailed analysis of segmentation metrics

Figures 5a and reffig:Figure5-b show scatter plots for segmentation-precision and segmentation-recall and for *correct detection* and *split* cases, respectively. These correspond to their respective columns of (a non-summarized version of) Table 3 with black and white dots representing the values of FCN-MN and SW detection models, respectively. The position of each dot in the plot corresponds to the mean segmentation-precision and mean segmentation-recall over all images in the test set, computed over the correctly detected components (splitted components, respectively) of the masks produced by the detection model associated to that dot. The standard deviation of the recall (precision) is shown as a horizontal (vertical) bar.

In Figure 5a (correct detections), one can observe that all black dots (FCN-MN) are clustered in the upper-right corner of the graph, enclosed by a minimum precision of approximately 65% and minimum recall of approximately 60%, while the white dots (SW) are clustered in the lower-right corner of the graph with maximum precisions of 50% and recall ranging from approximately 35% to 100%. Overall, both algorithms show relatively high recalls, but with FCN-MN reaching much larger precisions. We can point to the coarse detection of the SW positive patches as the main cause for low precision, as this is reduced when extra false positives are present in the positive mask.

In Figure 5b (splits), one can observe again the overwhelming improvements of FCN-MN over SW, with all (but one) SW cases presenting precisions under 60%, with the outlier showing a precision of nearly 70% and a similar distribution of recall values.

The segmentation results for the false alarm, the NA for each of the 27 models of FCN-MN and each of the 40 models of SW, i.e., for each cell in the one-before-last column of (a non-summarized version of) Table 3 are reported graphically. Figure 6 shows these results grouped in the form of two histograms, one for the FCN-MN detection models (black) and one for the SW models (white). Bars in the histogram represent the proportion of detection models whose mean NA (over all false alarm components of all images) falls within the bin interval. The more concentrated to the left the better the algorithm, as this indicates that more detection models for that algorithm resulted in smaller NA (on average). When compared to the histogram of SW, one can observe that the histogram for FCN-MN is considerably more concentrated towards the left, with all FCN-MN models concentrated in a single bar at the left-most interval of $[0.0, 1.0)$. For SW, the situation is rather different with bars at intervals as far to the right as $[57.0, 58.0)$, that is, detection models with areas as large as 58 times the bud area. These high values correspond to SW models with large window sizes such as 1000px with low thresholds, which results in components of big area (at least 1000x1000 px in the case of 1000px window size). As the SW detector relies on classifying regions as containing a bud or not, bigger window sizes yield bigger component areas.

3.2.3. Detailed analysis of localization metrics

To conclude, this subsection presents a graphical representation of the localization results reported in Table 3, that is, the *normalized distance* (ND)

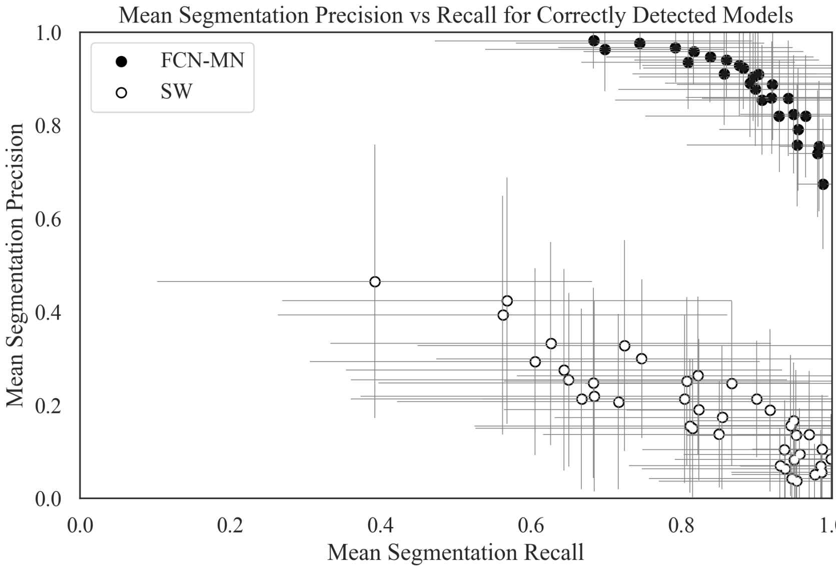

(a)

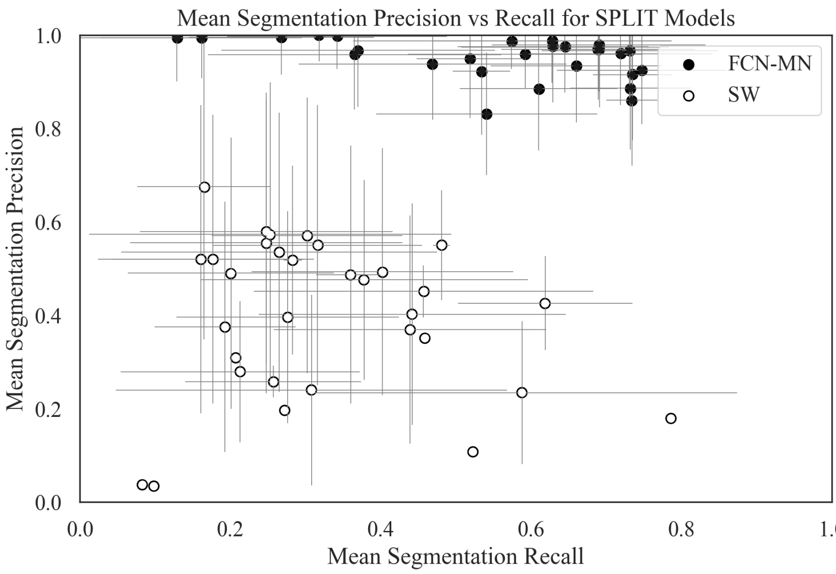

(b)

Figure 5: Segmentation Precision-Recall scatterplots reporting the results for FCN-MN and SW in black and white, respectively, with dots representing the segmentation precision and segmentation recall average over all images in the test set (and bars representing standard deviations) with one dot per hyper-parameter configuration (27 for FCN-MN and 40 for SW). In (a) averages were computed over the segmentation precision and recall of correctly detected components, while in (b), averages were computed over the segmentation precision and recall of split components. Recall and precision standard deviations are represented by the horizontal and vertical grey error bars.

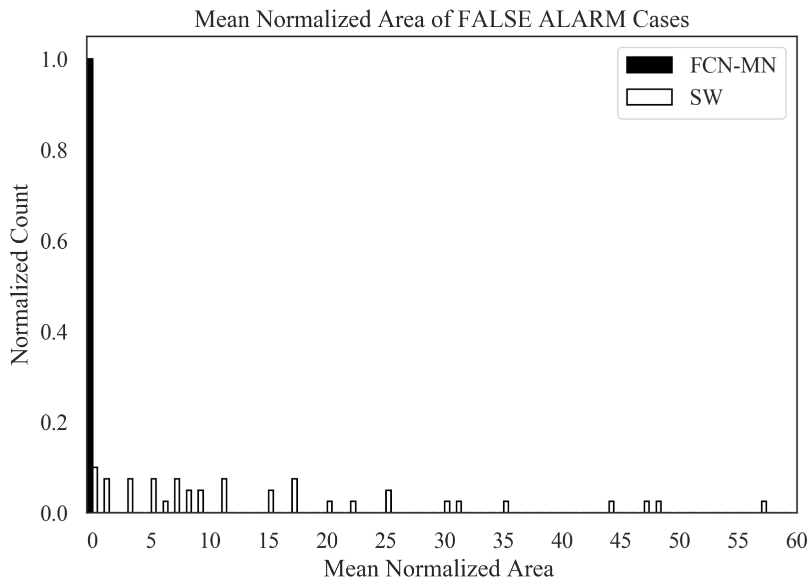

Figure 6: FCN-MN (black bars) and SW (white bars) histograms of the mean normalized area NA of false alarm components with bars representing the proportion of detection models whose mean NA falls within the bin interval.

only for false alarms. Figure 7 summarizes the ND values reported in the corresponding column of the (non-summarized version) of Table 3 in the form of two histograms, one for FCN-MN (black) and one for SW (white). Bars in the histogram represent the proportion of detection models (27 for FCN-MN and 40 for SW) whose mean ND falls within the bin interval. The more concentrated to the left the better the algorithm, as this indicates that more detection models for that algorithm resulted in smaller ND (on average). Here, again, the advantage of FCN-MN over SW is clear, with the histogram for FCN-MN more concentrated in the left-most part than that of SW, with the FCN-MN histogram running from the $(0, 1]$ to the $(7, 8]$ bin and the SW histogram running from the $(5, 6]$ towards the $(9, 10]$ bin; and their respective maximums are at $(3, 4]$ and $(7, 8]$, respectively, indicating that most FCN false alarms are at a distance of 3 to 4 bud diameters, while most SW's false alarms are at 7 to 8 bud diameters.

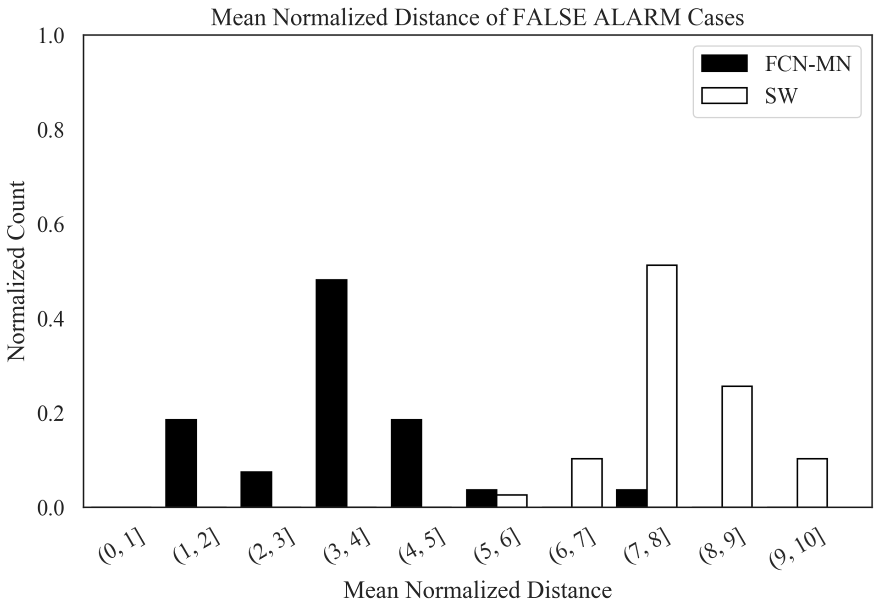

Figure 7: FCN-MN (black bars) and SW (white bars) histograms of mean normalized distance ND over all false alarm components with bars representing the proportion of detection models whose mean ND falls within the bin interval.

4. Discussion and Conclusions

Let us now discuss the results obtained by the proposed approach in the context of the problem of grapevine bud detection and its impact as a tool for measuring viticultural variables of interest, highlight the most important conclusions, and present future work.

In this work we introduce FCN-MN, a fully convolutional network with Mobile Net architecture for the detection of grapevine buds in 2D images captured in natural field conditions in winter (i.e., no leaves or bunches) and containing a maximum of one bud.

The experimental results confirmed our main hypothesis: that the detection quality achieved by FCN-MN is improved over the *sliding windows* detector (SW) in all three detection aspects: segmentation, correspondence identification and localization. Being SW the best bud detector known to these authors, one can conclude that FCN-MN is a strong contender in the state-of-the-art for bud detectors. However, even improving over these, one can still wonder if it can address the main *quality* requirements of a practical measurement of the bud-related variables in Table 1.

Quality performance could be assessed by the metrics reported in Table 3. In the best case, FCN-MN shows a detection-precision and detection-recall of 97.7% and 100%, respectively, a mean (and standard deviation) segmentation-precision and segmentation-recall for correct detections of 98.1%(0.6) and 98.8%(3.4), respectively, and for splits 99.9%(0.1) and 74.7%(28.1), respectively. For false alarms, it shows a minimum NA of 0.04(0.09) and a minimum ND of 0.04(0.22). However, each of these maximums correspond to different FCN-MN detectors. A better assessment must be conducted for a single detector. For that, we picked FCN-MN$^{0.6}_{16s}$ for its balanced quality overall. This detector reaches detection precision and recall of 95.6% and 93.6%, respectively, meaning than only 4.4% of all the detected connected components over all test images are false alarms, and that only 6.4% of all true buds could not be detected (i.e., resulted in detection failure). Additionally, it resulted in $S = 3$, meaning only 3 of all detections were splitted, which has a segmentation precision of 99.4%(0.6) and a segmentation recall of 16.2%(10.6) on average. The recall is rather small, suggesting that the split is, in fact, the result of pixel-wise detection of the bud so sparse that it became disconnected. In contrast, all remaining detections were correct (i.e., not splitted), reaching segmentation precisions of 92.2%(8.7), a rather similar value to that of splits, but a much larger mean segmentation recall of 88.2%(13.3). Overall, this resulted in a mean Dice measure for the correct detections of 89.1%(10.7), demonstrating a considerable (mean) coverage of the true bud with only 11.8% of the bud pixels missing (on average) and only 7.8% of the detected pixels covering the background (on average). The false alarm results for this detector showed an $NA = 0.08$ and $ND = 1.1$, showing that these components are rather small covering only an area that is 8% in size of the total bud area (on average) and distant to the true bud by only 1.1(0.65) diameters, on average.

Based on these results, what quality should one expect when the FCN-MN$^{0.6}_{16s}$ detector takes part in the measurement of the bud-related variables? For brevity, this point is discussed for three variables from Table 1: *bud number*, *bud area*, and *internode length*.

The case of *bud number*, for example, requires identifying correspondences for buds in the scene, so its quality will be impacted only by the metrics of detection precision and recall (95.6% and 93.6%, respectively). To evaluate this impact, we consider that a plant has approximately 240 buds on average. The number of buds per plant depends on many factors, such as training system, grape variety, type of treatment, time of year, among others, so this value is defined as indicative to achieve an approximate analysis. For this case, a detection precision of 95.6% would result in 11 buds counted in excess per plant, while a recall of 93.6% would result in the omission of 15 buds in the count.

In addition, this model produces 3 splits with two components each (according to our detailed observation of the results), i.e. a counting error of 3 buds in excess over the 140 true buds in the test set, representing an error of 2.1% approximately. Again, for the analysis of 240 buds per plant, it means that 5 buds would be counted in excess, giving a total of 16 buds counted in excess, practically cancelling out with the error of omission. But additionally, these errors could in practice be statistically characterized allowing for measurement correction towards more accurate values. Despite these good results, our approach still has practical limitations for the measurement of bud number due to the impossibility of automatically associating counts of the same bud in two different images, making it difficult to massively measure the bud count of a plant or plot.

The second variable of interest considered is *bud area*, where, in addition to identifying correspondences for the buds of a scene, it is necessary to segment it to estimate its area in pixels. Correspondence identification analysis is analogous to bud counting, so now only segmentation metrics are discussed. From the analysis developed in the previous paragraphs, it can be concluded that the segmentation errors by splits and false alarms have a low impact in the general results and, therefore, in the estimation of *bud area*. On the other hand, if we compensate the segmentation errors for the correct detections (i.e. 11.8% of the bud pixels missing and 7.8% of the detected pixels covering the background), the area estimation error is only 4%. For illustrative purposes, we see that this error is smaller than the precision error resulting from measuring the area of a bud with a caliper. If we assume that the shape of a bud fits a circle, and that the typical diameter of a bud is 5 mm, the resulting area is $19.63mm^2$. Since a caliper has an accuracy of $0.1mm$, the area precision error would be $\pm1.7mm^2$, equivalent to 8.6% of the total area, a figure that doubles the 4% error produced by our FCN-MN detector. To this difference, the error of manual measurement resulting from assuming a circular bud shape must be added, an unnecessary approximation in the case of FCN-MN.

As in the case of counting, these good results in measurement precision are limited to achieve a practical use of this type of measurement because it is impossible to automatically associate area measurements of the same bud in two different images, making it difficult to systematically measure this variable for the buds of a plant or plot. Furthermore, in this case, the areas obtained are in pixels, which need to be converted into length or area magnitudes.

Finally, let us consider the case of *internode length*, estimated by the distance between buds of the same branch (by the closeness between buds and nodes), which involves the operations of correspondence identification and localization. Again, correspondence identification analysis is analogous to bud counting, which in this case will result in the reporting of more than one distance due to the detection of more than one component per bud. Among these distances, we understand that the worst case can occur between false alarms –these being the farthest from the true bud– when they are at a distance of ND from the farthest side of the other bud. On average, it is $ND = 1.1$, which according to the typical diameter of vine buds is equivalent to about 5mm, a value much lower than the typical bud distances of approximately 15cm, i.e., about a 7.3% error in estimating the distance between buds/nodes. An important limitation of our approach for achieving a practical use of this measurement is the possibility of determining when two buds are on the same branch, which requires knowledge of the plant structure. Furthermore, with our method, only the distance projected in the image plane could be measured, which can arbitrarily differ from the actual distance in 3D.

The greatest impact errors occur because of the excess or omission of connected components, with the excess error exacerbated by the fact of associating detected buds with individual connected components. A possible improvement to mitigate these errors would be to apply some post-processing. One such post-processing is *spatial clustering* of connected components grouping them by proximity. One could expect this to improve the results based on the small areas of split and false alarm components. First, due to the closeness of the false alarms to the true bud (small ND) –as well as the splits and correctly detected components (overlapping with it)–, and the fact that true buds in real plants are typically tens or even hundreds of bud diameters apart, one could expect that a simple spatial clustering of the components would connect all of them together as a single, and correct, bud detection. Second, due to their small area -if clustered together- the false alarm components would only slightly reduce segmentation precision.

Another possible post-processing would be to rule out small connected components, for example, whose area in pixels normalized to the total detected area (sum of the areas of all connected components) is less than a certain threshold. Improvements could be expected with this post-processing, since the results in this work show that false alarms present small areas in relation to the true bud. Lastly, connected component filters could be considered based on plant structure, for example, ruling out connected components that are far away from (or do not overlap with) branches.

One could also consider in future works some improvements to overcome the limitations for practical use mentioned above: (i) no associations between plant parts of different images, (ii) distance and area measurements in pixels, (iii) only 2D geometry, (iv) lack of knowledge of underlying plant structure, and (v) need of images with no leaves.

One could also extend to buds the work of Santos et al. (2020) that addresses limitation (i) for grape bunches. Limitation (ii) could be easily addressed by adding to the visual scene some marker with known dimensions. This, however, requires such a marker in every image captured, a problem that could be overcome by first producing a calibrated 3D reconstruction of the scene, i.e., a 3D reconstruction calibrated with a single marker in one of its frames (Hartley and Zisserman, 2003; Moons et al., 2009). In this way, every 2D image could be calibrated against the 3D model, omitting the need for a marker. In addition, a 3D reconstruction of the scene could address limitation (iii) by locating the detected buds in 3D space, following, for instance, the approach taken by Díaz et al. (2018). Finally, a solution to limitations (iv) and (v) would require an integrated approach involving the detection in 3D of branches and leaves, respectively.

Acknowledgments

This work was funded by the Argentinean *Universidad Tecnológica Nacional* (UTN), the National Council of Scientific and Technical Research (CONICET), and the National Fund for Scientific and Technological Promotion (FONCyT).

References

Berenstein, R., Shahar, O.B., Shapiro, A., Edan, Y., 2010. Grape clusters and foliage detection algorithms for autonomous selective vineyard sprayer. Intelligent Service Robotics 3, 233–243.

Bramley, R.G., 2009. Lessons from nearly 20 years of precision agriculture research, development, and adoption as a guide to its appropriate application. Crop and Pasture Science 60, 197–217.

Chum, O., Zisserman, A., 2007. An exemplar model for learning object classes, in: 2007 IEEE Conference on Computer Vision and Pattern Recognition, IEEE. pp. 1–8.

Collins, C., Wang, X., Lesefko, S., De Bei, R., Fuentes, S., 2020. Effects of canopy management practices on grapevine bud fruitfulness. OENO One 54, 313–325.

Csurka, G., Dance, C., Fan, L., Willamowski, J., Bray, C., 2004. Visual categorization with bags of keypoints, in: Workshop on statistical learning in computer vision, ECCV, Prague. pp. 1–2.

Dalal, N., Triggs, B., 2005. Histograms of oriented gradients for human detection, in: 2005 IEEE Computer Society Conference on Computer Vision and Pattern Recognition (CVPR'05), pp. 886–893 vol. 1.

Diago, M.P., Correa, C., Millán, B., Barreiro, P., Valero, C., Tardaguila, J., 2012. Grapevine yield and leaf area estimation using supervised classification methodology on rgb images taken under field conditions. Sensors 12, 16988–17006.

Díaz, C.A., Pérez, D.S., Miatello, H., Bromberg, F., 2018. Grapevine buds detection and localization in 3d space based on structure from motion and 2d image classification. Computers in Industry 99, 303–312.

Dice, L.R., 1945. Measures of the amount of ecologic association between species. Ecology 26, 297–302.

Divvala, S.K., Hoiem, D., Hays, J.H., Efros, A.A., Hebert, M., 2009. An empirical study of context in object detection, in: 2009 IEEE Conference on computer vision and Pattern Recognition, IEEE. pp. 1271–1278.

Ferrari, V., Fevrier, L., Jurie, F., Schmid, C., 2007. Groups of adjacent contour segments for object detection. IEEE transactions on pattern analysis and machine intelligence 30, 36–51.

Garcia-Garcia, A., Orts-Escolano, S., Oprea, S., Villena-Martinez, V., Martinez-Gonzalez, P., Garcia-Rodriguez, J., 2018. A survey on deep learning techniques for image and video semantic segmentation. Applied Soft Computing 70, 41–65.

Grimm, J., Herzog, K., Rist, F., Kicherer, A., Töpfer, R., Steinhage, V., 2019. An adaptable approach to automated visual detection of plant organs with applications in grapevine breeding. Biosystems Engineering 183, 170–183.

Han, D., 2013. Comparison of commonly used image interpolation methods, in: Proceedings of the 2nd international conference on computer science and electronics engineering, Atlantis Press.

Hartley, R., Zisserman, A., 2003. Multiple view geometry in computer vision. Cambridge university press.

Herzog, K., Kicherer, A., Töpfer, R., 2014a. Objective phenotyping the time of bud burst by analyzing grapevine field images, in: XI International Conference on Grapevine Breeding and Genetics 1082, pp. 379–385.

Herzog, K., et al., 2014b. Initial steps for high-throughput phenotyping in vineyards. Australian and New Zealand Grapegrower and Winemaker , 54.

Hirano, Y., Garcia, C., Sukthankar, R., Hoogs, A., 2006. Industry and object recognition: Applications, applied research and challenges, in: Toward category-level object recognition. Springer, pp. 49–64.

Howard, A.G., Zhu, M., Chen, B., Kalenichenko, D., Wang, W., Weyand, T., Andreetto, M., Adam, H., 2017. Mobilenets: Efficient convolutional neural networks for mobile vision applications. arXiv preprint arXiv:1704.04861 .

Jaccard, P., 1912. The distribution of the flora in the alpine zone. 1. New phytologist 11, 37–50.

Kahng, M., Andrews, P.Y., Kalro, A., Chau, D.H.P., 2017. A cti v is: Visual exploration of industry-scale deep neural network models. IEEE transactions on visualization and computer graphics 24, 88–97.

Kaymak, Ç., Uçar, A., 2019. A brief survey and an application of semantic image segmentation for autonomous driving, in: Handbook of Deep Learning Applications. Springer, pp. 161–200.

Kliewer, W.M., Dokoozlian, N.K., 2005. Leaf area/crop weight ratios of grapevines: influence on fruit composition and wine quality. American Journal of Enology and Viticulture 56, 170–181.

Kornblith, S., Shlens, J., Le, Q.V., 2019. Do better imagenet models transfer better?, in: Proceedings of the IEEE conference on computer vision and pattern recognition, pp. 2661–2671.

Lampert, C.H., Blaschko, M.B., Hofmann, T., 2008. Beyond sliding windows: Object localization by efficient subwindow search, in: 2008 IEEE conference on computer vision and pattern recognition, IEEE. pp. 1–8.

Litjens, G., Kooi, T., Bejnordi, B.E., Setio, A.A.A., Ciompi, F., Ghafoorian, M., Van Der Laak, J.A., Van Ginneken, B., Sánchez, C.I., 2017. A survey on deep learning in medical image analysis. Medical image analysis 42, 60–88.

Long, J., Shelhamer, E., Darrell, T., 2015. Fully convolutional networks for semantic segmentation, in: Proceedings of the IEEE conference on computer vision and pattern recognition, pp. 3431–3440.

Lorenz, D., Eichhorn, K., Bleiholder, H., Klose, R., Meier, U., Weber, E., 1995. Growth stages of the grapevine: Phenological growth stages of the grapevine (vitis vinifera l. ssp. vinifera)—codes and descriptions according to the extended bbch scale. Australian Journal of Grape and Wine Research 1, 100–103.

Lowe, D.G., 2004. Distinctive image features from scale-invariant keypoints. International journal of computer vision 60, 91–110.

Matese, A., Di Gennaro, S.F., 2015. Technology in precision viticulture: A state of the art review. International journal of wine research 7, 69–81.

May, P., 2000. From bud to berry, with special reference to inflorescence and bunch morphology in vitis vinifera l. Australian Journal of Grape and Wine Research 6, 82–98.

Moons, T., Van Gool, L., Vergauwen, M., 2009. 3D Reconstruction from Multiple Images: Principles. Now Publishers Inc.

Ning, C., Zhou, H., Song, Y., Tang, J., 2017. Inception single shot multibox detector for object detection, in: 2017 IEEE International Conference on Multimedia & Expo Workshops (ICMEW), IEEE. pp. 549–554.

Noyce, P.W., Steel, C.C., Harper, J.D., Wood, R.M., 2016. The basis of defoliation effects on reproductive parameters in vitis vinifera l. cv. chardonnay lies in the latent bud. American Journal of Enology and Viticulture 67, 199–205.

Nuske, S., Achar, S., Bates, T., Narasimhan, S., Singh, S., 2011. Yield estimation in vineyards by visual grape detection, in: 2011 IEEE/RSJ International Conference on Intelligent Robots and Systems, IEEE. pp. 2352–2358.

Oguz, I., Carass, A., Pham, D.L., Roy, S., Subbana, N., Calabresi, P.A., Yushkevich, P.A., Shinohara, R.T., Prince, J.L., 2017. Dice overlap measures for objects of unknown number: application to lesion segmentation, in: International MICCAI Brainlesion Workshop, Springer. pp. 3–14.

Pan, S.J., Yang, Q., 2009. A survey on transfer learning. IEEE Transactions on knowledge and data engineering 22, 1345–1359.

Pérez, D.S., Bromberg, F., Diaz, C.A., 2017. Image classification for detection of winter grapevine buds in natural conditions using scale-invariant features transform, bag of features and support vector machines. Computers and electronics in agriculture 135, 81–95.

Rowley, H.A., Baluja, S., Kanade, T., 1996. Human face detection in visual scenes, in: Advances in Neural Information Processing Systems, pp. 875–881.

Rudolph, R., Herzog, K., Töpfer, R., Steinhage, V., 2018. Efficient identification, localization and quantification of grapevine inflorescences in unprepared field images using fully convolutional networks. arXiv preprint arXiv:1807.03770 .

Sánchez, L.A., Dokoozlian, N.K., 2005. Bud microclimate and fruitfulness in vitis vinifera l. American Journal of Enology and Viticulture 56, 319–329.

Santos, T.T., de Souza, L.L., dos Santos, A.A., Avila, S., 2020. Grape detection, segmentation, and tracking using deep neural networks and three-dimensional association. Computers and Electronics in Agriculture 170, 105247.

Seng, K.P., Ang, L.M., Schmidtke, L.M., Rogiers, S.Y., 2018. Computer vision and machine learning for viticulture technology. IEEE Access 6, 67494–67510.

Shelhamer, E., Long, J., Darrell, T., 2017. Fully convolutional networks for semantic segmentation. IEEE transactions on pattern analysis and machine intelligence 39, 640–651.

Shorten, C., Khoshgoftaar, T.M., 2019. A survey on image data augmentation for deep learning. Journal of Big Data 6, 60.

Siam, M., Gamal, M., Abdel-Razek, M., Yogamani, S., Jagersand, M., 2018. Rtseg: Real-time semantic segmentation comparative study, in: 2018 25th IEEE International Conference on Image Processing (ICIP), IEEE. pp. 1603–1607.

Simonyan, K., Zisserman, A., 2015. Very deep convolutional networks for large-scale image recognition. CoRR abs/1409.1556.

Tardaguila, J., Diago, M., Blasco, J., Millán, B., Cubero, S., García-Navarrete, O., Aleixos, N., 2012. Automatic estimation of the size and weight of grapevine berries by image analysis, in: Proc. CIGR AgEng.

Tardáguila, J., Diago, M.P., Millan, B., Blasco, J., Cubero, S., Aleixos, N., 2012. Applications of computer vision techniques in viticulture to assess canopy features, cluster morphology and berry size, in: I International Workshop on Vineyard Mechanization and Grape and Wine Quality 978, pp. 77–84.

Tarry, C., Wspanialy, P., Veres, M., Moussa, M., 2014. An integrated bud detection and localization system for application in greenhouse automation, in: 2014 Canadian Conference on Computer and Robot Vision, IEEE. pp. 344–348.

The Australian Wine Research Institute, a. Viticare on Farm Trials - Manual 3.1: Measuring Fruit Quality. 1 ed. The Australian Wine Research Institute. Accessed August 2020.

The Australian Wine Research Institute, b. Viticare on Farm Trials - Manual 3.3: Vine Health. 1 ed. The Australian Wine Research Institute. Accessed August 2020.

Tilgner, S., Wagner, D., Kalischewski, K., Velten, J., Kummert, A., 2019. Multi-view fusion neural network with application in the manufacturing industry, in: 2019 IEEE International Symposium on Circuits and Systems (ISCAS), IEEE. pp. 1–5.

Vapnik, V., 2013. The nature of statistical learning theory. Springer science & business media.

Wang, X., Han, T.X., Yan, S., 2009. An hog-lbp human detector with partial occlusion handling, in: 2009 IEEE 12th international conference on computer vision, IEEE. pp. 32–39.

Whalley, J., Shanmuganathan, S., 2013. Applications of image processing in viticulture: A review .

Whelan, B., McBratney, A., Viscarra Rossel, R., 1996. Spatial prediction for precision agriculture, in: Proceedings of the Third International Conference on Precision Agriculture, Wiley Online Library. pp. 331–342.

Xu, S., Xun, Y., Jia, T., Yang, Q., 2014. Detection method for the buds on winter vines based on computer vision, in: 2014 Seventh International Symposium on Computational Intelligence and Design, IEEE. pp. 44–48.

Zhao, F., Rong, D., Liping, L., Chenlong, L., 2018. Research on stalk crops internodes and buds identification based on computer vision. MS&E 439, 032080.